Range – Cocone equation with Doppler parameter for SAR imagery positioning

CHENG Chunquan, ZHANG Jixian, HUANG Guoman, ZHANG Li

Chinese Academy of Surveying and Mapping, Beijing 100830, *China*

Abstract: In this paper we analyze the geometry mechanism of Synthetical Aperture Radar(SAR) imaging, and propose the Range-Cocone equation with Doppler parameter(RCD) for SAR imagery positioning taking linear and angular elements as orientation parameters. A serial of tests are taken that include orientation with single image, free-net adjustment without Ground Control Point(GCP), block adjustment with sparse GCPs, and block adjustment with self-calibration parameters. The test datasets covered a part of Dengfeng suburb are 99 airborne SAR images with 0.5 m resolution and non-zero doppler parameter. Compared to R-D model, the presented RCD model decreases the number of orientation parameters and is convenient for adjustment combining SAR imagery with POS data. RCD based block adjustment model with self-calibration parameters can increase the accuracy greatly in the case where SAR sensor is not calibrated, or calibrated coarsely Tests also indicate that the airborne SAR imagery and the proposed positioning model can meet the accuracy requirement for aerial triangulation at the scale of 1∶ 5000/1∶ 10000 over hill and mountainous areas with sparse GCPs.

Key words: SAR imagery positioning, Range-Cocone equation with Doppler frequency, block adjustment, aerial triangulation, exterior orientation elements, self-calibration

CLC number: P237 **Document code:** A

Citation format: **Cheng C Q, Zhang J X, Huang G M and Zhang L. 2013. Range-Cocone equation with Doppler parameter for SAR imagery positioning. Journal of Remote Sensing, 17(6): 1444 – 1458 [DOI: 10.11834/jrs.20132332]**

1 INTRODUCTION

Positioning with remote sensing imagery is to get the two or three-dimensional space information of ground targets corresponding to image by geometry processing. The geometric positioning of remote sensing image mainly includes geometric c orrection, three-dimensional stereo positioning and block adjustment. Based on rigorous sensor model, accuracy of the inter-o rientation parameters and exterior orientation parameter of image can be greatly improved by aerial triangulation, which is the key technology for rigorous positioning with remote sensing image.

The rigorous geometric imaging model of the radar image is mainly based on sensor state vector and Doppler parameters, or the model is based on state vector and attitude parameters (exterior orientation elements). The R-D and Leberl model are the main format of the former class, where R-D model takes account of non-zero doppler frequency, and it has a clear geometric physical meaning for SAR imagery (Johnsen, 1995). The R-D equation is shown as

$$\begin{cases} \sqrt{(X-Xs)^2+(Y-Ys)^2+(Z-Zs)^2}-R=0 \\ 2\left[(X-Xs)V_{Xs}+(Y-Ys)V_{Ys}+(Z-Zs)V_{Zs}\right]/ \\ \quad (\lambda R)-f_D=0 \end{cases} \tag{1}$$

where (X,Y,Z) and $(Xs,Ys,Zs,V_{Xs},V_{Ys},V_{Zs})$ are the ground point coordinates and the state vector of antenna center of SAR sensor; λ, f_D, and R are SAR wavelength, Doppler frequency, and measurement distance of the radar wave, respectively.

Though positions and attitudes of radar sensor change d uring the data acquisition and radar wave is affected by the p ositions and attitudes, the equation for beam center plane can still be established according to the invariable relationship b etween beam center and the sensor. From view point of the r adar imaging geometry, Cheng, et al. (2012) build Range-C oplanarity (R-Cp) equation for real aperture (or equivalent real aperture) radar image, and the apparent functional form o f R-Cp equation (Cheng and Zhang, 2012) can be described as

$$\begin{cases} x=\left[(X-Xs)(\cos\varphi\cos\kappa)+(Y-Ys)\sin\kappa-\right. \\ \quad \left.(Z-Zs)\right]/M_a=0 \\ y=\left[\sqrt{(X-Xs)^2+(Y-Ys)^2+(Z-Zs)^2}-R_0\right]/M_r \end{cases} \tag{2}$$

where M_a and M_r are pixel sizes in azimuth and range directions; R_0 is the initial slant range; y is the column coordinate of the p ixel on the image; (φ,κ) are the attitude angles.

Orientation parameters in Eq. (2) is consistent with collinear equation for optical images, and some mature photogrammetric techniques and methods for the optical images can be conveniently applied for radar iamges. However, the model is based on imaging mechanism of real aperture radar. For SAR imagery, even

Received: 2012-12-03; **Accepted:** 2013-02-25; **Version of record first published:** 2013-03-04

Foundation: Natural Science Foundation of China (No. 41071237); National High Technology Research and Development Program (863 Program) (No. 2011AA120401, 2011AA120402)

First author biography: CHENG Chunquan (1972—), male, Ph. D., associate professor. He is studying for digital photogrammetry of optical and SAR imagery. E-mail: cspring@casm.ac.cn

if the same raw signal data is used, the image deformation is different using different motion compensations and focusing values; similarly, even if the same SAR imagery and state vector data are used, positioning results is different using different doppler in geometric processing. Therefore, Range-Coplanarity and collinear equation are limited in some SAR imagery positioning.

At present, geometry correction techniques of SAR imagery have been widely studied in different cases (Yuan & Wu, 2010; Zhang, 2010); although the block adjustment technology is studied (Toutin, 2003; Huang, et al., 2008; Ma, et al., 2010), a chievements are still rarely, and block adjustment technologies and methods of SAR imagery that meet the mapping production demands at large scale with sparse GCPs are still lacking. If the applications of the Range-Coplanarity equation is extended to all SAR imagery imaging with R-D model, and can replace the R-D model for the combined adjustment of multisource data and meet the requirements for large scale mapping, it would be significative for enhancing data processing theory and application level of SAR imagery.

2 GEOMETRIC ANALYSIS OF SAR IMAGING WITH R-D MODEL

The SAR imaging geometry has obvious differences from real aperture radar images. SAR imaging is related to motion compensation and signal focus in addition to the sensor parameters and the sensor state during data obtaining. It is complicated to establish geometric imaging equation directly associated with signal imaging model and methods. However, according to R-D imaging mechanism, the spatial geometric relationship between the sensor and the target can still be rebuilt. For arbitrary image points, they meet the Doppler equation conditions, namely:

$$f_D = \frac{2\boldsymbol{V} \cdot \boldsymbol{SP}_i}{\lambda \mid \boldsymbol{SP}_i \mid} = \frac{2 \mid \boldsymbol{V} \mid \boldsymbol{V} \cdot \boldsymbol{SP}_i}{\lambda \mid \boldsymbol{V} \mid \mid \boldsymbol{SP}_i \mid} \tag{3}$$

where $\boldsymbol{V}$ is the vector for the relative velocity between the sensor and the target, $\boldsymbol{SP}_i$ is the vector from sensor to target corresponding to the image point. Therefore, they have the following relationship:

$$\frac{\boldsymbol{V} \cdot \boldsymbol{SP}_i}{\mid \boldsymbol{V} \mid \mid \boldsymbol{SP}_i \mid} = \lambda f_D / (2 \mid \boldsymbol{V} \mid) \tag{4}$$

where $|\boldsymbol{V}|$ is the scalar of the velocity.

Assuming the angle between the vector $\boldsymbol{SP}_i$ from the sensor to the target point and the velocity vector $\boldsymbol{V}$ is θ, there is:

$$\cos\theta = \frac{\boldsymbol{V} \cdot \boldsymbol{SP}_i}{\mid \boldsymbol{V} \mid \mid \boldsymbol{SP}_i \mid} = \lambda f_D / (2 \mid \boldsymbol{V} \mid) \tag{5}$$

Eq. (5) shows that corresponding ground points of SAR i magery pixels with any given Doppler are on the rotation cone (Fig. 1(a)—Fig. (d)), which takes SAR sensor $\boldsymbol{S}$ as vertex, the vector of velocity $\boldsymbol{V}$ as rotation axis, and $\theta(\theta = 90° - \tau)$ as semiapex angle. We call the cone as SAR Doppler cone corresponding to an image point.

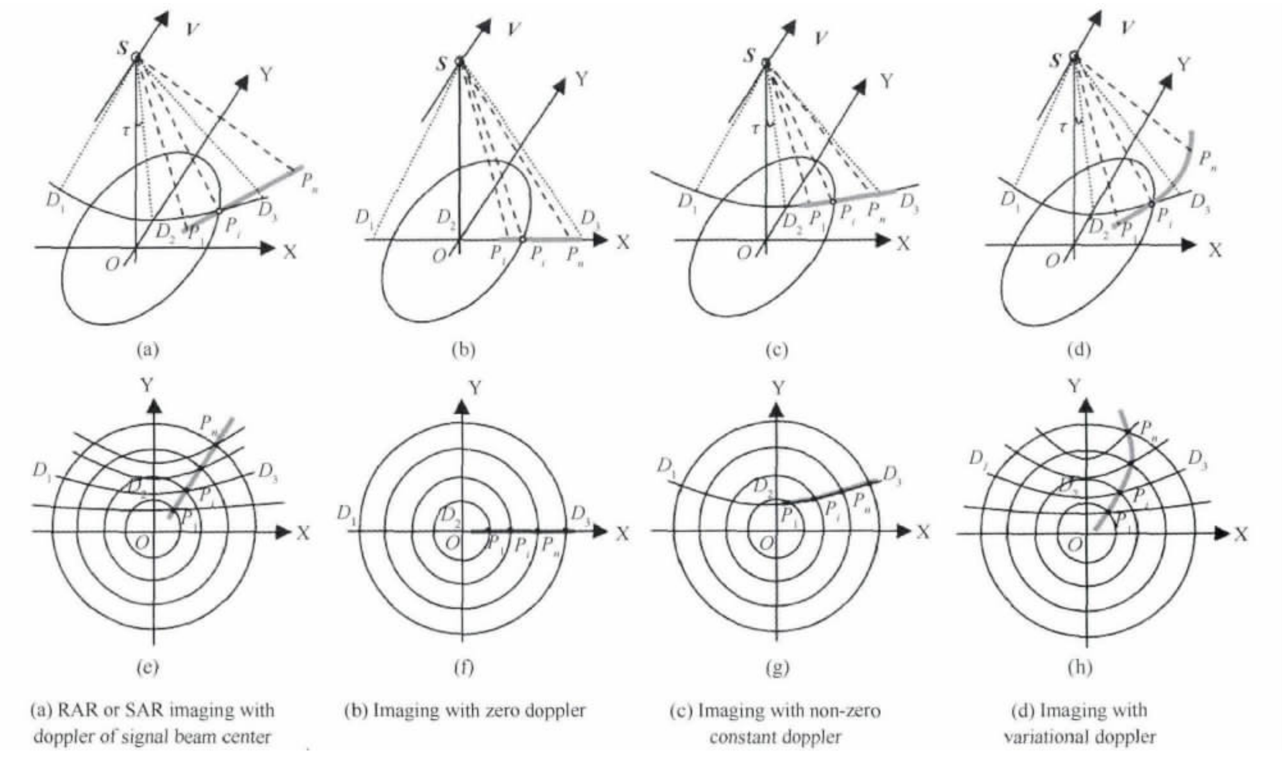

Fig. 1 Imaging geometry sketch map for range line pixels

Assuming there are successively image pixels P_1, P_i and P_n from near-range to far-range on one range line of SAR imagery. For Real Aperture Radar (RAR), the line image is obtained from signal beam within one transmission, and the corresponding ground target points of the line pixels are inevitable on the wave plane (scanning with plane mode, Fig. 1 (a) $\boldsymbol{S} - P_1P_iP_n$) or cone surface (scanning with cone mode, Fig. 1(c) $\boldsymbol{S} - P_1P_iP_n$) and pass the s ensor location $\boldsymbol{S}$. For SAR imagery imaging with R-D model, ground point position P_i corresponding to image pixel p_i is d etermined by Doppler equation (doppler cone $\boldsymbol{S}$ −

$D_1D_2D_3$ in Fig. 1(a)—Fig. 1(d)), range equation ($S-P_i$ sphere taking $\boldsymbol{S}$ as the center and range measured by radar as radius in Fig. 1(a)—F ig. 1(d)), and Earth ellipsoid equation (the intersection set b etween the range equation and ellipsoid equation is the circle O $-P_i$ in Fig. 1(a)—Fig. (d)). So for range line pixels $P_1P_iP_n$, their corresponding ground point $P_1P_iP_n$ and sensor location $\boldsymbol{S}$ have difference spatial geometric relationships when SAR imaging with difference Doppler:

(1) Imaging with doppler of signal beam center over the t arget point: this imaging mode is usually applied on spaceborne SAR imagery with sensor smoothly running, such as one mode for TerraSAR (DLR, 2007). Under the conditions of the non o rthogonal-side-looking, Doppler cones of each pixels are different, but the target point and the sensor position are still in plane $\boldsymbol{S}-P_1P_iP_n$ of beam center emitting by SAR sensor, so R-Cp model can still be applied on the rigorous SAR imagery positioning, and target point set $P_1P_iP_n$ is line (Fig. 1(a), Fig. 1(e)).

(2) Imaging with zero doppler: For semiapex angle θ is 90°, doppler cone becomes plane perpendicular to the velocity vector, and it indicates that the sensor position and corresponding ground target point are in the plane $\boldsymbol{S}-P_1P_iP_n$, and target point set $P_1P_iP_n$ is a straight line (Fig. 1(b), Fig. 1(f)).

(3) Imaging with a non-zero constant doppler: it means that the sensor and ground target corresponding to all the line pixels are on the same doppler cone $\boldsymbol{S}-P_1P_iP_n$, and the target point set $P_1P_iP_n$ is hyperbola (intersection set of cone and earth-ellipsoid) (Fig. 1(c), Fig. 1(g)).

(4) Imaging with arbitrariness doppler: Doppler cones of different pixels are different, and the surface formed by line set from sensor to all targets is an irregular curved surface, and the target point set $P_1P_iP_n$ is on an irregular curve (Fig. 1(d), F ig. 1(h)).

As it can be seen from the above analysis, SAR imagery with R-D signal imaging is different from real aperture radar, and the shape of ground targets set $P_1P_iP_n$ corresponding to range line pixels is related to imaging doppler. Assuming these target points are scanned by a beam from a pseudo real aperture radar sensor, the shape of the beam $\boldsymbol{S}-P_1P_iP_n$ is consequently i ntent to change with different doppler.

For real aperture radar image, sensor state vector and attitudes and terrain determine doppler of signal. The position, v elocity and attitude of SAR sensor during data acquisition are different from the value after motion compensation of SAR i maging. Doppler value from SAR signal beam center and Doppler value from focused image parameters are not always the same. SAR imagery positioning is directly related to the compensated sensor state vector and attitude, and is related to the reference oppler used in imaging.

3 RANGE-COCONE EQUATION WITH DOPPL ER PARAMETERS (RCD) FOR SAR IMAG ING GEOMETRY

3.1 Range-Cocone equation with Doppler para-m eters

Taking sensor state vector and attitude as orientation parameters, Cocone equation with Doppler parameter is built in a ccordance with the fact that ground point P_i corresponding to an image point p_i and SAR sensor location S are on doppler cone.

Assuming the X axis of the platform coordinate system after rotation with attitude angle φ-κ-ω is consistent with the direction of the compensated velocity, and $\boldsymbol{i}$ is the unit vector of the X -axis, doppler cone equation can be built as same as Cheng, e t al. (2012):

$$\cos_i\theta = [i_X(X-Xs) + i_Y(Y-Ys) + i_Z(Z-Zs)] / |\boldsymbol{SP}_i| \tag{6}$$

where θ is semiapex angle of the cone, $|\boldsymbol{SP}_i| = \sqrt{(X-Xs)^2+(Y-Ys)^2+(Z-Zs)^2}$; $\boldsymbol{i} = [i_X \quad i_Y \quad i_Z]$ is unit vector of body coordinate system X-axis after attitude rotation. According to Cheng, et al. (2012), we can have:

$$\boldsymbol{i} = [i_X \quad i_Y \quad i_Z] = R(\varphi,\kappa)[1,0,0]^{\mathrm{T}} = [\cos\varphi\cos\kappa \sin\kappa - \sin\varphi\cos\kappa] \tag{7}$$

With Eq. (5), Eq. (6) and Eq. (7), Cocone equation can be written as

$$\cos\varphi\cos\kappa(X-Xs) + \sin\kappa(Y-Ys) - \sin\varphi\cos\kappa(Z-Zs) - |\boldsymbol{SP}_i|\lambda f_{\mathrm{D}}/2|\boldsymbol{V}| = 0 \tag{8}$$

Meantime, for SAR imagery, there is the range equation:

$$|\boldsymbol{SP}_i| = R \tag{9}$$

where R is the range measured by radar wave, according to coordinate y in range-line, the pixel size of slant-range M_{r} and initial slant-range R_0 of SAR imagery it can be calculated: $R = R_0 + M_{\mathrm{r}}y$.

Substituting $|\boldsymbol{SP}_i| = R$ of the range equation into Eq. (8), the Cocone equation can be further simplified. Together with expansion equation of the range Eq. (9), and range-Cocone equation with Doppler parameter for SAR imaging geometry can be o btained as

$$\begin{cases} (X-Xs)^2 + (Y-Ys)^2 + (Z-Zs)^2 = R^2 \\ \cos\varphi\cos\kappa(X-Xs) + \sin\kappa(Y-Ys) - \\ \quad \sin\varphi\cos\kappa(Z-Zs) = R\lambda f_{\mathrm{D}}/2|\boldsymbol{V}| \end{cases} \tag{10}$$

The Eq. (8) is a cone equation, and the second equation of the Eq. (10) is a plane equation. This plane equation adds a c onstant-item $R\lambda f_{\mathrm{D}}/2|\boldsymbol{V}|$ compared with the co-planarity equation in Cheng, et al. (2012). When f_{D} does not equal to 0, the plane is no longer passing the antenna center of SAR sensor. When it is used for SAR imagery, the positions and attitudes are values after motion compensation, it means that attitudes are no longer directly related to the original value of IMU measured, but are related to the attitudes after motion compensation. Though the plane is still perpendicular to the X-axis after attitude rotation, the X-axis is not consistent with the X-axis of actual platform body coordinate system, but consistent with direction of X-axis or velocity after motion compensation. Range-Cocone e quation with Doppler parameters is called as RCD equation in this paper to be distinguished from the $\mathrm{RC_P}$ equation.

3.2 RCD equation with the form of apparent function and in geocentric rectangular coordinate system

Refering to Cheng and Zhang (2012), both sides of the plane Eq. (10) are divided by $M_{\mathrm{a}}\cos\beta$, where β is the angle b etween the velocity and the X-axis of the platform c oordinate system. For the X -axis of the compensated platform coordinate system and the velocity have same vector direction, therefore cos β

=1, and there is apparent function of RCD equation with image point coordinates as d ependent variable:

$$\begin{cases} x = [\cos\varphi\cos\kappa(X - Xs) + \sin\kappa(Y - Ys) - \\ \quad \sin\varphi\cos\kappa(Z - Zs) - R\lambda f_D/2|\boldsymbol{V}|]/M_a = 0 \\ y = [\sqrt{(X - Xs)^2 + (Y - Ys)^2 + (Z - Zs)^2} - \\ \quad R_0]/M_r \end{cases} \tag{11}$$

The attitude values from the Eq. (11) is related to velocity after imaging motion compensation and attitude reference coordinate system. The initial value of attitude angle can be calculated according to the two physical parameters. Because the choice of attitude reference coordinate system can be arbitrary, as shown in Cheng and Zhang (2012), we used the flight coordinate system as attitude reference and set 0 to both φ and κ as initial value. Meanwhile, in view of the conversion relationship between the attitude reference coordinate system and the geocentric rectangular coordinate system, RCD equation in geocentric r ectangular coordinate system can be established:

$$\begin{cases} x = [i_X \cdot (X - Xs) + i_Y \cdot (Y - Ys) + i_Z \cdot (Z - Zs) - \\ \quad R\lambda f_D/2|\boldsymbol{V}|]/M_a = 0 \\ y = [\sqrt{(X - Xs)^2 + (Y - Ys)^2 + (Z - Zs)^2} - R_0]/M_r \end{cases} \tag{12}$$

where $\boldsymbol{i} = [i_X \quad i_Y \quad i_Z]^T = \boldsymbol{R}_V^E \boldsymbol{R}_b^V(\varphi,\kappa,\omega)[1 \quad 0 \quad 0]^T$

$$\begin{bmatrix} i_X \\ i_Y \\ i_Z \end{bmatrix} = \boldsymbol{R}_V^E R_b^V = \begin{bmatrix} (X_V)_X & (Y_V)_X & (Z_V)_X \\ (X_V)_Y & (Y_V)_Y & (Z_V)_Y \\ (X_V)_Z & (Y_V)_Z & (Z_V)_Z \end{bmatrix} \begin{bmatrix} \cos\varphi\cos\kappa \\ \sin\kappa \\ -\sin\varphi\cos\kappa \end{bmatrix} =$$

$$\begin{bmatrix} (X_V)_X\cos\varphi\cos\kappa + (Y_V)_X\sin\kappa - (Z_V)_X\sin\varphi\cos\kappa \\ (X_V)_Y\cos\varphi\cos\kappa + (Y_V)_Y\sin\kappa - (Z_V)_Y\sin\varphi\cos\kappa \\ (X_V)_Z\cos\varphi\cos\kappa + (Y_V)_Z\sin\kappa - (Z_V)_Z\sin\varphi\cos\kappa \end{bmatrix} \tag{13}$$

where $\boldsymbol{R}_b^V$ is transformation matrix from platform coordinate s ystem to flight coordinate system; $\boldsymbol{R}_V^E$ is transformation matrix from flight coordinate system to geocentric rectangular coordinate system, the subscript X, Y and Z of (X_V), (Y_V) and (Z_V) are respectively component of tri-axial unit vector of the flight coordinate system in tri-axial directions of the geocentric rectangular coordinate system.

Taking sensor positions (Xs, Ys, Zs), attitudes (φ, κ), the ground point coordinates (X, Y, Z) and azimuth and range system errors $(\Delta x_0, \Delta y_0)$ of the sensor calibration parameters as unknowns and linearizing the RCD equation, we can obtain the general form of error equation for SAR imagery observation:

$$\begin{cases} v_x = f_{xXs}\mathrm{d}Xs + f_{xYs}\mathrm{d}Ys + f_{xZs}\mathrm{d}Zs + f_{x\varphi}\mathrm{d}\varphi + f_{x\kappa}\mathrm{d}\kappa - \\ \quad f_{xXs}\mathrm{d}X - f_{xYs}\mathrm{d}Y - f_{xZs}\mathrm{d}Z + \Delta x_0 - l_x \\ v_y = f_{yXs}\mathrm{d}Xs + f_{yYs}\mathrm{d}Ys + f_{yZs}\mathrm{d}Zs + f_{y\varphi}\mathrm{d}\varphi + f_{y\kappa}\mathrm{d}\kappa - \\ \quad f_{yXs}\mathrm{d}X - f_{yYs}\mathrm{d}Y - f_{yZs}\mathrm{d}Z + \Delta y_0 - l_y \end{cases} \tag{14}$$

where (v_x, v_y) is error correction of image point coordinates; (l_x, l_y) is constant term of error equation; f_* is coefficient of error e quation.

As it can be seen from the Eq. (14), error equation of SAR imagery is still consistent with the general form of the error e quation of colinearity equation, only differing in linearization. From the Cocone equations in Eq. (11) Eq. (12), we can build the error propagation Eq. (15) for influence of Doppler error on image point coordinate error.

$$\mathrm{d}x = \frac{-R\lambda}{2M_a|\boldsymbol{V}|}\mathrm{d}f_D \tag{15}$$

Eq. (15) means the influence of Doppler error on image g eometry positioning cannot be ignored.

4 COMBINED ADJUSTMENT MODEL FOR SAR IMAGERY AND ORBIT-ATTITUDES OR POS DATA

Three sensor position parameters (Xs, Ys, Zs) and three velocity parameters $(\boldsymbol{V}_{Xs}, \boldsymbol{V}_{Ys}, \boldsymbol{V}_{Zs})$ are used as exterior orientation parameters for R-D model positioning. Pang (2006) has shown that the velocity in the elevation direction is very sensitive to the elevation accuracy. Orientation parameter number of RCD model can be reduced to five, which could improve the stability and r eliability of adjustment solver for triangulation specially under the conditions of sparse GCPs.

Low-order polynomial was used as the refined model for the attitudes and positions (Cheng & Zhang, 2012).

$$\begin{cases} Xs = Xs_0 + a_0 + a_1 t \\ Ys = Ys_0 + b_0 + b_1 t \\ Zs = Zs_0 + c_0 + c_1 t \\ \varphi = \varphi_0 + f_0 + f_1 t \\ \kappa = \kappa_0 + g_0 + g_1 t \end{cases} \tag{16}$$

where Xs, Ys, Zs, φ and κ are exterior orientation parameters after refinement; Xs_0, Ys_0, Zs_0, φ_0 and κ_0 are the initial values of exterior orientation parameters; a_i, b_i, c_i, f_i, g_i $(i=0,1)$ are polynomial coefficients of orbit attitude error correction.

Substituting correction model into the imaging model, and taking the refined model parameters a_i, b_i, c_i, f_i and g_i $(i=0, 1)$, the ground point coordinates dX, dY, dZ and sensor system error parameters Δx_0, Δy_0 as unknowns, we can get the linearized error equation.

The systematic error correction parameters $(\Delta x_0, \Delta y_0)$ in a zimuth and range direction of all images can be used as g eometric calibration parameters for SAR sensors. Two kinds of block adjustment models are established, and the first one takes sensor position, attitude correction model parameters and the ground point coordinates as unknowns:

$$\begin{cases} \boldsymbol{V}_{xy} = \boldsymbol{B}_g g + \boldsymbol{B}_t t - \boldsymbol{L}_{xy} & \text{Weight}: P_{xy} \\ \boldsymbol{V}_g = \boldsymbol{E}_g g - \boldsymbol{L}_g & \text{Weight}: P_g \\ \boldsymbol{V}_t = \boldsymbol{E}_t t - \boldsymbol{L}_t & \text{Weight}: P_t \end{cases} \tag{17}$$

Self-calibration parameters $\boldsymbol{s}(\Delta x_0, \Delta y_0)$ for SAR sensor are added to the second model as unknowns and observations:

$$\begin{cases} \boldsymbol{V}_{xy} = \boldsymbol{B}_g g + \boldsymbol{B}_t t + \boldsymbol{B}_s \boldsymbol{s} - \boldsymbol{L}_{xy} & \text{Weight}: P_{xy} \\ \boldsymbol{V}_g = \boldsymbol{E}_g g - \boldsymbol{L}_g & \text{Weight}: P_g \\ \boldsymbol{V}_t = \boldsymbol{E}_t \boldsymbol{t} - \boldsymbol{L}_t & \text{Weight}: P_t \\ \boldsymbol{V}_s = \boldsymbol{E}_s \boldsymbol{s} - \boldsymbol{L}_s & \text{Weight}: P_s \end{cases} \tag{18}$$

In the Eq. (17) and Eq. (18), $\boldsymbol{V}_{xy}$, V_g, $\boldsymbol{V}_t$ and $\boldsymbol{V}_s$ are error e quations of the coordinates of image points, the coordinates of the ground points, orbit-attitude (or POS) and SAR sensor calibration observation; $\boldsymbol{g}$ is unknowns $[dX, dY, dZ]$ of ground point coordinate incremental; $\boldsymbol{t}$ is vector of unknowns $[a_i, b_i, c_i, f_i, g_i]$ $(i=0,1)$ of orbit-attitude (or POS) correction polynomial model coefficients; $\boldsymbol{s}$ represents the unknown vector $(\Delta x_0, \Delta y_0)$ of s ystem error of SAR sensor calibration parameters; $\boldsymbol{B}_g$, $\boldsymbol{B}_t$, $\boldsymbol{E}_g$, $\boldsymbol{E}_t$, and $\boldsymbol{E}_s$ are coefficient matrix of unknowns.

5 POSITIONING TEST AND ANALYSIS FOR AIRBORNE SAR IMAGERY

5.1 Test data

Test site is located at Dengfeng suburb, Henan province. The area covered 13 km × 13 km with terrain elevation in the range from 230 m and 440 m. X-band airborne SAR data was obtained by multi-band multi-polarization interferometric polarimetric CASMSAR mapping system developed by Chinese Academy of Surveying and Mapping (Zhang, 2012).

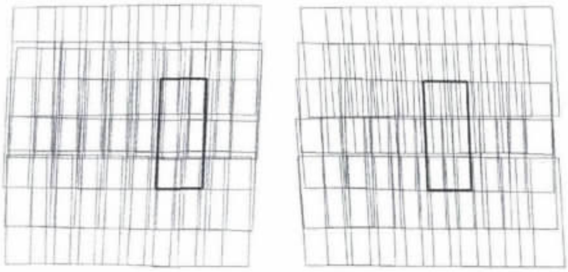

(a) East flight-line images (b) West flight-line images

Fig.2 East and west flight-line block images for the same area (broad-brush is boundary of one image frame)

Fig.3 A zoom-in of CASMSAR intensity images

There are six east flight-lines and five west flight-lines and each flight-line including 9 or 10 scene images and there are 55 scene images from east flight-line and 44 scenes from west flight-line overall. There have large Doppler differences in signal focusing among different strips ranging from −600 Hz and 6 00 Hz; the pixel size in azimuth and slant range are respectively 0.31 m and 0.25 m and its actual ground resolution is about 0 .5—1.0 m, the SAR wavelength is 0.03 m, the near-range is a bout 2600 m and the far-range is about 7500 m. The flight height of the plane is about 3000 m. Fig. 2 shows the relationship of scenes from east flight-line and west flight-line, and Fig. 3 shows a zoom-in of the intensity image frame.

5.2 Test

(1) Orientation with one scene

One of the images (the imaging Doppler frequency of this scene is −322 Hz) and its original auxiliary data are used to test orientation accuracy without GCP (Table 1). Here Lebel F model, R-D model, RCD model and R-Cp model are adopted for test r espectively. From the view of imaging geometry, orientation differences of non-zero Doppler SAR imagery can be examined with different models.

For R-Cp model, pitch angle is −0.785 degrees and yaw a ngle −3.44°. These parameters were taken from the original POS observed value of the image. The calculation of orientation residual (v_y) with range equation in R-D model is same as RCD and RCp model. And the calculation of azimuth residual v_x can follow Cheng and Zhang (2012). Both sides of the Doppler e quation in Eq. (1) are multiplied by the coefficient $c = \lambda R/(2|V|M_a)$, which can be converted to the form of apparent Eq. (19) with x, y as the dependent variable. the solution of v_x, v_y can be made from error equation of the function. The calculation method of orientation residual with Leberl F equation is same as R-D equation, but the value of f_D is set to constant 0.

$$\begin{cases} x = 2c \cdot [(X - Xs)V_{Xs} + (Y - Ys)V_{Ys} + (Z - Zs)V_{Zs}] / (\lambda R_j) - c \cdot f_D = 0 \\ y = [\sqrt{(X - Xs)^2 + (Y - Ys)^2 + (Z - Zs)^2} - R_0] / M_r \end{cases} \tag{19}$$

Table 1 Accuracy statistics of orientation with different models /pixels

Dot mark/Range coordinate	P01		P02		P03		P04		P05	
Image point coordinate (line/column)	7454	4502	4867	8359	4358	10759	54	12465	662	17916
Direction of error	Vx	Vy	Vx	Vy	Vx	Vy	Vx	Vy	Vx	Vy
Leberl F	485.33	7.43	605.23	9.95	684.58	10.75	734.60	11.10	914.93	11.87
R-D	2.75	7.43	−3.10	9.95	−1.97	10.75	−7.57	11.10	−4.85	11.87
R-Cp	175.52	7.43	39.36	9.95	−25.65	10.75	−76.22	11.10	−194.38	11.87
RCD	2.75	7.43	−3.10	9.95	−1.97	10.75	−7.57	11.10	−4.85	11.87

(2) Free-net block adjustment

Here the scenes from east flight-lines and bidirectional (including east and west) flight-lines separate were taken as test data. And Eq. (17) is used for the free-net adjustment without GCP, and statistics results are filled in "state vector" line and "0" c olumn in Table 2. As a comparison, the original orientation parameters without correction are used for positioning with block images, and Residual Mean Squares (RMS) is 2.73 m in plane and 2.35 m in elevation from east flight-lines, and RMS is 2 .08 m in plane and 2. 91 m in elevation from bidirectional flight-lines.

(3) Block adjustment with different GCPs

The test data here are same as test (2) including east flight-lines and bidirectional flight-lines. But GCPs are used in the mapping area and the GCP number is changed from 1 to 15. D ifferent GCP configurations were designed as:

Table 2 Block adjustment accuracy statistics with different positioning models and methods /m

	Orientation parameters	GCP number		0	1	4	5	9	15
East flight-lines	State vector	Control points	Plane		0.07	0.51	0.60	1.13	1.31
			Elevation		0.11	0.44	0.49	0.74	0.97
		Check points	Plane	2.19	2.04	1.75	1.69	1.55	1.47
			Elevation	1.97	1.35	1.21	1.19	1.11	1.00
	State vector and self-calibration parameters	Control points	Plane		0.19	0.39	0.43	1.06	1.31
			Elevation		0.17	0.33	0.40	0.78	0.93
		Check points	Plane	2.14	2.03	1.61	1.58	1.50	1.44
			Elevation	1.91	1.22	1.10	1.06	1.01	0.95
		Maximum error	Plane	3.50	2.89	2.37	2.25	2.17	1.95
			Elevation	3.92	2.33	2.19	2.16	2.05	2.00
Bidirectional flight-lines	State vector	Control points	Plane		0.02	0.39	0.42	0.67	0.88
			Elevation		0.03	0.22	0.27	0.38	0.51
		Check points	Plane	1.40	1.31	1.15	1.11	1.02	0.93
			Elevation	1.61	0.80	0.72	0.72	0.61	0.53
	State vector and self-calibration parameters	Control points	Plane		0.09	0.41	0.49	0.75	0.83
			Elevation		0.03	0.38	0.40	0.42	0.49
		Check points	Plane	1.30	1.17	1.05	0.97	0.92	0.87
			Elevation	0.59	0.58	0.55	0.53	0.50	0.46
		Maximum error	Plane	2.30	2.14	2.03	2.06	1.85	1.77
			Elevation	1.19	1.11	1.02	0.99	0.92	0.89

Case 1: one GCP centered at the test area;

Case 2: 4 GCPs with one at each corner of the test area;

Case 3: 5 GCPs with 1 at the center and the rest 4 at the four corners;

Case 4: 9 GCPs evenly distributed as 3 rows and 3 columns;

Case 5: 15 GCPs evenly distributed.

Dfferent case has different influence on block adjustment accuracy, and statistic results are shown in "state vector" row and "1", "4", "5", "9", "15" columns of "GCP number" in Table 2.

(4) Block adjustment with self-calibration parameters

Here Δx_0 and Δy_0 in RCD error Eq. (14) were taken as self-calibration parameter of SAR sensor, and Eq. (18) are used for tests. The free-net adjustment and block adjustment with the same data and ways in test (2) and test (3) were practices. The statistics accuracy was filled in the rows of "state vector and self-calibration parameters" in Table 2.

5.3 Test analysis

(1) From orientation accuracy with R-D model and original auxiliary data of the scene, it can be seen that there is a small e rror in azimuth, and larger error in range, but the standard deviation from azimuth is bigger than that from range. It also shows there exits systematic error in range and random error in azimuth.

(2) When doppler frequency of SAR image is non-zero and large, orientation errors with different geometry models have d istinct difference. Here the accuracy of R-D and RCD model is best, and their errors in both direction are identical. While the a ccuracy of R-Cp model is relatively poor, and Leber F model the worst.

(3) Compared to the positioning test with the uncorrected o riginal auxiliary data, the accuracy in plane and elevation are improved by adjustment with no or sparse GCP. Under the same conditions the accuracy of block adjustment with self-calibration parameters is higher than that of block adjustment without self-calibration parameters, and the block adjustment accuracy of SAR imagery with bidirectional flight-line images is higher than that of east flight-line images alone.

(4) With the increase of the number of GCPs, the positioning accuracy of check points is increased correspondingly. But the accuracy is not improved rapidly. The reason is that the random error of image distortion make the influence of GCPs on images weakening, the influence from GCP can't be propagated for long-range and each GCP can only affects few neighborhood images.

(5) For the adjustment with only east flight-line images, the positioning accuracy is not ideal. It is because the imaging errors and matching errors have a great influence on elevation accuracy when positioning with small base-height-ratio stereo images. All these indicate that more work is needed to improve the clarity of images and reduce random errors from imaging.

(6) When adjustment with bidirectional flight-line images and self-calibration adjustment model, a better positioning accuracy can be reached even with sparse or no GCPs. It indicates that the model and method can effectively eliminate the system error from sensor or imaging. When the GCP number is up to five, it meets block adjustment accuracy required by 1∶5000 and 1∶10000 mapping criterion over hill and mountain (AQSIQ & SAC, 1992).

6 CONCLUSION

This paper together with the theses (Cheng, et al., 2012;

Cheng & Zhang 2012) systematically discussed the rigorous s ensor model based on the sensor position and attitude parameters for the real aperture radar and SAR imagery. Range-Coplanarity (R-Cp) equation can be used for real aperture radar imagery scanning with plane mode, SAR imagery imaging with signal doppler of beam center, or SAR imagery imaging with zero doppler. Range-CoCone (R-Cc) (Cheng, et al., 2012) can be used for real aperture radar imagery scanning with cone mode or SAR imagery imaging with non-zero constant Doppler. And RCD model can be applied to all radar (including real aperture radar and SAR) imagery imaging with R-D model.

Compared with R-D model, RCD equation proposed in this study reduces the number of the orientation parameters which can reduce the correlation between the orientation parameters and improve the stability of adjustment solver. With image point coordinate (x, y) as dependent variable and exterior paraments $(Xs, Ys, Zs, \varphi, \kappa)$ as independent variable, the form of apparent function of RCD still can absorb some mature digital photogrammetric technologies and methods from optical line array images when SAR imagery triangulation processing, and realize combined adjustment among SAR image data and POS data. Block adjustment model with self-calibration parameters has an important role in improving image positioning accuracy under the condition of poor geometric calibration accuracy to SAR s ensor. At the same time, although there still has room to improve the positioning accuracy along with the upgrade of a irborne SAR mapping system, the aerial triangulation accuracy of airborne SAR imagery with sparse GCP has reached the r equirements of 1∶ 5000 and 1∶ 10000 aerial m apping criterion over hills and mountains area. Airborne SAR mapping system and airborne SAR imagery will gradually be a pplied to mapping at large scale.

REFERENCES

AQSIQ, SAC (General Administration of Quality Supervision, Inspection and Quarantine of the People's Republic of China, and Standardization Administration of the People's Republic of China), Specifications for aerophotogrammetric office operation 1∶ 5000、1∶ 10000 topographic maps. GB/T 13990-92

Cheng C Q and Zhang J X. 2012. Rigorous positioning with side-looking radar imagery based on Range-Coplanarity model. Journal of Remote Sensing, 16(5): 881-894

Cheng C Q, Zhang J X, Deng K Z and Zhang L. 2012. Range-Coplanarity equation for radar geometric imaging. Journal of Remote Sensing, 16(1): 38-49

DLR (The German Aerospace Center). 2007. CAF-Cluster Applied Remote Sensing. TerraSAR-X Ground Segment Level 1b Product Format Specification. http://www.astrium-geo.com/files/pmedia/public/r460_9_030201_level-1b-product-format-specification_1.3.pdf

Huang G M, Yue X J, Zhao Z and Fan H D. 2008. Block adjustment with airborne SAR images based on polynomial otho-rectification. Geomatics and Information Science of Wuhan University, 33(6): 569-572

Johnsen H, Lauknes L and Guneriussen T. 1995. Geocoding of fast-delivery ERS-1 SAR image mode product using DEM data. International Journal of Remote Sensing, 16(11): 1957-1968 [DOI: 10.1080/01431169508954532]

Ma J, You H J, Long H and Ding C B. 2010. A new method of block adjustment of airborne SAR images with few GCPs. Journal of Electronics and Information Technology, 32(12): 2842-2847

Toutin T. 2003. Path processing and block adjustment with RADARSAT-1 SAR images. IEEE TGARS, 41(10): 2320-2328 [DOI: 10.1109/TGRS.2003.814661]

Pang L. 2006. Study of the Triangulation Method from Airborne Synthetic Aperture Radar Images. Qingdao: Shandong University of Science and Technology: 20-46

Yuan X X and Wu Y D. 2010. Object location of space-borne SAR imagery under lacking ground control points. Geomatics and Information Science of Wuhan University, 35(1): 88-91

Zhang G, Qiang Q, Zhu X Y and Tang X M. 2010. Ortho-rectification of Satellite-borne SAR image based on image simulation. Acta Geodaetica et Cartographica Sinica, 39(6): 554-559

Zhang J X, Zhao Z, Huang G M and Lu Z. 2012. CASMSAR: An Integrated Airborne SAR Mapping System. PHOTOGRAMMETRIC ENGINEERING & REMOTE SENSING (11): 1111-1114

考虑多普勒参数的 SAR 影像距离—共面方程及其定位

程春泉，张继贤，黄国满，张力

中国测绘科学研究院 对地观测技术国家测绘局重点实验室，北京 100830

摘 要:通过对合成孔径雷达(SAR)影像成像几何机理的分析,以传感器位置和姿态作为定向参数,构建了考虑多普勒参数的 SAR 影像距离—共面方程及基于该方程的 SAR 影像空中三角测量模型。以登封地区 99 景 0.5 m 分辨率机载非 0 多普勒 SAR 影像为试验数据,进行了单片定向、无控制点的自由网平差、稀少控制点的区域网平差及带有自检校参数的区域网平差等系列试验。与 R-D 模型相比,本文模型减少了定向参数的数目,实现了 SAR 影像与 POS 数据的联合平差处理,建立的带有自检校参数的 SAR 影像区域网平差模型,对提高稀少或无地面控制点条件下未进行(或低精度)几何定标 SAR 影像的区域网平差精度起到了显著作用。较少控制点条件下模型满足了丘陵和山区 1: 5000/1: 10000 航摄测图对空中三角测量精度的要求。

关键词:SAR 影像定位,距离—共面方程,区域网平差,空中三角测量,多普勒频率,外方位元素

中图分类号:P237 文献标志码:A

引用格式:程春泉,张继贤,黄国满,张力. 2013. 考虑多普勒参数的 SAR 影像距离—共面方程及其定位. 遥感学报,17(6):1444 - 1458

Cheng C Q, Zhang J X, Huang G M and Zhang L. 2013. Range-Cocone equation with Doppler parameter for SAR imagery positioning. Journal of Remote Sensing, 17(6): 1444 - 1458 [DOI: 10.11834/jrs.20132332]

1 引 言

遥感影像的定位是指通过对遥感影像的处理,获得影像对应的地面目标的平面或 3 维空间信息。遥感影像的几何定位主要包括几何纠正、立体定位和区域网平差加密、影像地理信息产品生产等内容。以几何构像模型为基础,通过平差处理,实现定向参数精度的提高是遥感影像定位的关键技术。

雷达影像的严密几何构像模型主要有基于传感器状态矢量和多普勒参数的模型,以及基于传感器状态矢量和姿态参数(外方位元素)的模型两种形式。R-D 模型和 F. Leberl 是前者的主要模型,其中 R-D 模型考虑了多普勒频率非 0 值情况,具有明确的几何物理意义 (Johnsen,1995)。R-D 方程表达式如下:

$$\begin{cases} \sqrt{(X-Xs)^2+(Y-Ys)^2+(Z-Zs)^2}-R=0 \\ 2[(X-Xs)V_{Xs}+(Y-Ys)V_{Ys}+(Z-Zs)V_{Zs}]/ \\ \quad (\lambda R)-f_D=0 \end{cases} \tag{1}$$

式中,(X,Y,Z)、$(Xs,Ys,Zs,V_{Xs},V_{Ys},V_{Zs})$为地面点坐标和 SAR 传感器天线中心状态矢量,$\lambda$、$f_D$、$R$ 分别为 SAR 波长、多普勒频率及雷达波测量距离。

我们(程春泉 等,2012;程春泉和张继贤,2012)分别从构像几何和数据处理的角度构建了真实孔径和等效真实孔径侧视雷达平面扫描模式的距离—共面方程。它们根据传感器位置和姿态在数据获取过程中虽然变化但传感器发射的波束中心面与传感器间的相对关系不变的事实来建立,波束面方程由传感器位置和姿态参数确定。距离—共面方程为:

$$\begin{cases} x=[(X-Xs)(\cos\varphi\cos\kappa)+(Y-Ys)\sin\kappa- \\ \quad (Z-Zs)]/M_a=0 \\ y=[\sqrt{(X-Xs)^2+(Y-Ys)^2+(Z-Zs)^2} \\ \quad -R_0]/M_r \end{cases} \tag{2}$$

式中,M_a、M_r 分别为方位向和距离向像元大小,R_0 为初始斜距,y 为像元在影像上的列坐标,(φ,κ)为姿态角。

收稿日期:2012-12-03;修订日期:2013-02-25;优先数字出版日期:2013-03-04

基金项目:国家自然科学基金(编号:41071237);国家高技术研究发展计划(863 计划)(编号:2011AA120401, 2011AA120402)

第一作者简介:程春泉(1972—),男,博士,副研究员,主要从事航空航天光学与雷达遥感影像摄影测量理论与应用研究。E-mail: cspring@casm.ac.an

与雷达共线方程模型一样,上述方程的优点表现为:外定向参数与光学影像共线方程一致,且能方便利用一些光学影像成熟的摄影测量技术和方法。但该模型建立在真实孔径雷达影像成像几何关系上,没有考虑 SAR 影像信号成像聚焦因素。对于 SAR 影像,即使是采用相同的原始信号数据,采用不同的运动补偿和多普勒值成像时,所获得的影像形变是不同的;同样,即使是采用相同的 SAR 影像和传感器状态,几何处理采用不同的多普勒值,定位结果也是不同的,不含多普勒参数的距离—共面模型没有考虑多普勒对 SAR 影像定位的影响,在非 0 多普勒 SAR 影像几何处理应用中受到限制。

目前,SAR 影像在不同情况下的纠正技术得到了广泛研究(袁修孝和吴颖丹,2010;张过,2010);而对于区域网平差技术,国内外虽有研究(Toutin,2003;黄国满 等,2008;马婧 等,2010),但总体上相关成果仍然很少,能够满足中大比例尺测图应用需求的稀少控制点 SAR 影像区域网平差技术和方法仍然缺乏。如果将距离—共面方程的应用范围延伸到所有 R-D 成像的 SAR 影像,使其能够替代 R-D 模型进行多源数据的联合处理,满足中大比例尺测图要求,对提升 SAR 影像数据处理理论和应用水平,无疑有重要的意义。为了建立这种模型,本文首先对任意多普勒参数 R-D 模型成像的 SAR 影像几何特征进行分析。

2 R-D 模型成像 SAR 构像几何分析

SAR 影像构像几何关系与真实孔径雷达影像有明显的区别,SAR 影像除与传感器参数和传感器获取数据时的状态有关外,还与信号成像联系在一起。目前,我们还难以将几何处理模型与信号成像模型及信号成像方法建立直接联系。但根据 SAR 影像 R-D 成像机理,仍能重建传感器与目标间的空间几何关系。对任意像点,满足多普勒方程条件:

$$f_D = \frac{2\boldsymbol{V}\cdot\boldsymbol{SP}_i}{\lambda|\boldsymbol{SP}_i|} = \frac{2|\boldsymbol{V}|\ \boldsymbol{V}\cdot\boldsymbol{SP}_i}{\lambda|\boldsymbol{V}||\boldsymbol{SP}_i|} \tag{3}$$

故有等式:

$$\frac{\boldsymbol{V}\cdot\boldsymbol{SP}_i}{|\boldsymbol{V}||\boldsymbol{SP}_i|} = \lambda f_D/(2|\boldsymbol{V}|) \tag{4}$$

式中,$|\boldsymbol{V}|$ 为传感器与目标间的相对速度大小,$\boldsymbol{SP}_i$ 为传感器至地面目标的矢量。

设传感器到目标点的矢量与速度矢量间的夹角为 θ,则有:

$$\cos\theta = \frac{\boldsymbol{V}\cdot\boldsymbol{SP}_i}{|\boldsymbol{V}||\boldsymbol{SP}_i|} = \lambda f_D/(2|\boldsymbol{V}|) \tag{5}$$

式(5)表明,对于任意给定多普勒参数值的 SAR 影像像点,其对应的地面点在 SAR 传感器 S 为顶点、以速度 V 方向为旋转轴、半顶角为 θ($\theta=90°-\tau$)的旋转锥面上(图 1(a)—(d)),我们将这个锥面称为对应像点的 SAR 多普勒锥面。

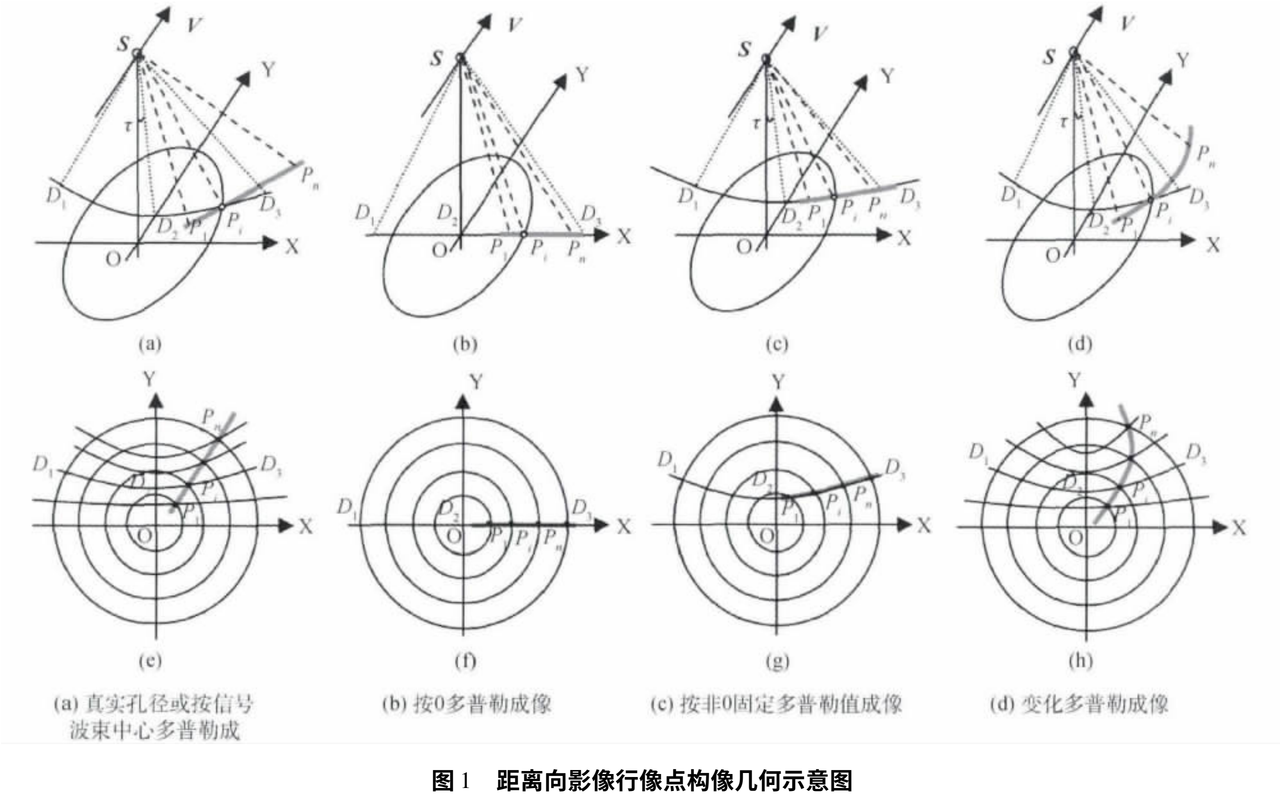

图 1 距离向影像行像点构像几何示意图

假设影像某一距离行上由近距到远距依次有像点 P_1、P_i 和 P_n。对于真实孔径雷达，该行影像由一次发射的波束信号获得，影像对应的目标点必然在此次信号发射时经过传感器位置 S 的波束平面（平面扫描模式，图 1(a) 中 $S\text{-}P_1P_iP_n$）或锥面（锥面扫描模式，图 1(c) 中 $S\text{-}P_1P_iP_n$）上。而对于 R-D 模型成像的 SAR 影像，任意一像点 P_i 对应地面点位置 P_i 由多普勒方程（对应图 1(a)—(d) 中多普勒曲面 $S\text{-}D_1D_2D_3$）、距离方程（对应图中球心在 S，半径为雷达测量距离为 SP_i 的球，图 1(a)—(d) 以及地球椭球模型共同决定（其中距离方程与椭球方程的交集为圆心为 O 的距离圆 O-P_i，图 1(a)—(d)）。而一行影像 $P_1P_iP_n$ 的几何构像，根据 SAR 成像多普勒的不同，传感器空间位置 S 及地面点 $P_1P_iP_n$ 间有如下相应的空间几何关系：

（1）按波束中心过目标点的多普勒成像：这种成像方式一般应用在传感器运行平稳的星载 SAR 影像中，如 TerraSAR 的一种成像方式（DLR，2007）。在非正侧视条件下每个像点对应的多普勒锥面是不同的，但目标点与传感器位置仍然在传感器发射的信号波束中心面 $S\text{-}P_1P_iP_n$ 内，R-Cp 模型仍可应用于这种 SAR 影像的严密定位，目标点集 $P_1P_iP_n$ 为直线（图 1(a)(e)）；

（2）按固定的 0 多普勒成像：多普勒曲面变成垂直于速度向量的平面，表明传感器位置与所有影像行对应的地面目标点均在平面 $S\text{-}P_1P_iP_n$ 内，目标点集 $P_1P_iP_n$ 为直线（图 1(b)(f)）；

（3）按某个固定的非 0 多普勒成像：表明传感器位置与所有影像行对应的地面目标点均在一个相同的多普勒锥面 $S\text{-}P_1P_iP_n$ 上，目标点集 $P_1P_iP_n$ 为双曲线的一支（图 1(c)(g)）；

（4）按任意多普勒成像：不同像点对应的多普勒锥面是不同的，目标点集与传感器位置间的连线所构成的面是一个不规则的曲面，目标点集 $P_1P_iP_n$ 在一条不规则的曲线上（图 1(d)(h)）。

从以上分析中可以看出，与真实孔径雷达不同，对于 R-D 模型成像的 SAR 影像，一行影像对应的地面定位点 $P_1P_iP_n$ 组成的形状与成像所采用的多普勒参数值有关，不是固定的。假设这些点由一个虚拟的真实孔径雷达传感器的某个波束扫描，则波束曲面 $S\text{-}P_1P_iP_n$ 的形状也不是固定的。

对于真实孔径雷达影像，传感器状态矢量、姿态和地形决定了波束信号的多普勒值。而 SAR 传感器在数据获取时的位置、速度和姿态与 SAR 成像时运动补偿后对应的值是不同的，SAR 信号波束中心的多普勒值与聚焦成像采用的多普勒值也不一定是相同的。SAR 影像构像几何与运动补偿后的传感器状态矢量、姿态和成像聚焦采用的多普勒值直接相关。

3 考虑多普勒参数的 SAR 影像距离—共面方程数据结果处理与分析

3.1 方程推导

以传感器状态矢量和姿态为定向参数的非 0 多普勒 SAR 影像共面（锥面）方程根据任意像点 $p_i(x_i, y_i)$ 对应的地面点 $P_i(X,Y,Z)$ 在以 SAR 传感器位置 $S(Xs,Ys,Zs)$ 为顶点的 SAR 多普勒锥面上这一条件来构建。

设载机平台本体坐标系在三姿态角均为 0 时三轴指向与物方参考坐标系三轴一致，X 轴经过姿态角 $\varphi\text{-}\kappa\text{-}\omega$ 旋转后与运动补偿后的速度方向一致，则地面点在以载机平台本体坐标系 X 轴为中心轴的锥面内。设 $\boldsymbol{i}$ 为姿态旋转后本体坐标系 X 轴的单位向量，参考文献（程春泉 等，2012）中锥面方程的构建方法，有：

$$\cos\theta = [i_X(X-Xs)+i_Y(Y-Ys)+i_Z(Z-Zs)]/|\boldsymbol{SP}_i| \tag{6}$$

式中，$|\boldsymbol{SP}_i| = \sqrt{(X-Xs)^2+(Y-Ys)^2+(Z-Zs)^2}$，$\theta$ 为锥面的半顶角；$\boldsymbol{i} = [i_X \quad i_Y \quad i_Z]$ 为姿态旋转后的本体坐标系 X 轴单位向量（程春泉和张继贤，2012）：

$$\boldsymbol{i} = [i_X \quad i_Y \quad i_Z] = R(\varphi,\kappa)[1,0,0]^{\mathrm{T}} = [\cos\varphi\cos\kappa \quad \sin\kappa \quad -\sin\varphi\cos\kappa] \tag{7}$$

根据式（5）—（7），有共面（锥面）方程：

$$\cos\varphi\cos\kappa(X-Xs)+\sin\kappa(Y-Ys)-\sin\varphi\cos\kappa(Z-Zs)-|\boldsymbol{SP}_i|\lambda f_{\mathrm{D}}/2|V| = 0 \tag{8}$$

同时，对于 SAR 影像，有距离方程：

$$|\boldsymbol{SP}_i| = R \tag{9}$$

式中，R 为雷达波的测量距离，可根据 SAR 影像距离向列坐标 y、斜距像元大小 M_r 和初始斜距 R_0 计算：$R = R_0 + M_r y$

将距离方程中的 $|\boldsymbol{SP}_i| = R$ 代入锥面式（8）中，共面（锥面）方程进一步简化。与距离式（9）展开式一起，得出考虑多普勒参数的 SAR 影像的距离—共面（锥面）方程：

$$\begin{cases}(X-Xs)^2+(Y-Ys)^2+(Z-Zs)^2 = R^2 \\ \cos\varphi\cos\kappa(X-Xs)+\sin\kappa(Y-Ys)- \\ \sin\varphi\cos\kappa(Z-Zs) = R\lambda f_{\mathrm{D}}/2|\boldsymbol{V}|\end{cases} \tag{10}$$

式(8)表达的是一个锥面方程,但式(10)中的第二式表达的却是一个平面方程。该平面方程与程春泉等人(2012)推导的平面方程相比,形式上加了一个常数项 $R\lambda f_D/2|\boldsymbol{V}|$。表明当 f_D 不等于 0 时,平面不再经过 SAR 传感器天线中心位置。方程应用于 SAR 影像定位时,位置和姿态值也不再与 POS 测量得到的原始值直接相关,而是与运动补偿后的值有关。即平面虽然仍垂直于 X 轴方向,但 X 轴方向不是与实际航飞时载机平台本体坐标系姿态旋转后的 X 轴一致,而是与成像运动补偿后的平台本体坐标系 X 轴或运动补偿后的速度方向一致。为了与前文有所区分,本文将考虑多普勒参数的距离—共面(锥面)方程简称为 RCD(Range-Cocone e quation involved Doppler parameter)方程。

3.2 显函数形式及地心直角坐标系中的 RCD 方程

式(10)平面方程的两边同时除以 $M_a\cos\beta$,(β 为速度与传感器载体平台坐标系的 X 轴间的夹角)方程仍然成立(程春泉和张继贤,2012)。同时,本文姿态旋转后的本体坐标系 X 轴与速度方向一致,故 $\cos\beta=1$,有像点坐标为因变量、传感器位置和姿态为自变量的 RCD 方程显函数形式:

$$\begin{cases} x = [\cos\varphi\cos\kappa(X-Xs)+\sin\kappa(Y-Ys)- \\ \quad \sin\varphi\cos\kappa(Z-Zs)-R\lambda f_D/2|\boldsymbol{V}|]/M_a=0 \\ y = [\sqrt{(X-Xs)^2+(Y-Ys)^2+(Z-Zs)^2} \\ \quad -R_0]/M_r \end{cases} \tag{11}$$

式中,姿态角与成像运动补偿后的速度和姿态参考坐标系有关,即姿态角初值可以根据这两个物理量反算。由于姿态参考坐标系的选择是任意的(程春泉和张继贤,2012),以飞行坐标系作为姿态参考坐标系,则姿态俯仰角 φ 和偏航角 κ 初值均为 0。同时,根据姿态参考坐标系与地心直角坐标系间的转换关系,可以建立地心直角坐标系中的 RCD 方程:

$$\begin{cases} x = [i_X\cdot(X-Xs)+i_Y\cdot(Y-Ys)+i_Z\cdot \\ \quad (Z-Zs)-R\lambda f_D/2|\boldsymbol{V}|]/M_a=0 \\ y = [\sqrt{(X-Xs)^2+(Y-Ys)^2+(Z-Zs)^2} \\ \quad -R_0]/M_r \end{cases} \tag{12}$$

式中,

$$\boldsymbol{i}=[i_X \quad i_Y \quad i_Z]^{\mathrm{T}}=\boldsymbol{R}_V^E\boldsymbol{R}_b^V(\varphi,\kappa,\omega)[1 \quad 0 \quad 0]^{\mathrm{T}}。$$

$$\begin{bmatrix} i_X \\ i_Y \\ i_Z \end{bmatrix} = \boldsymbol{R}_V^E R_b^V = \begin{bmatrix} (X_V)_X & (Y_V)_X & (Z_V)_X \\ (X_V)_Y & (Y_V)_Y & (Z_V)_Y \\ (X_V)_Z & (Y_V)_Z & (Z_V)_Z \end{bmatrix}\begin{bmatrix} \cos\varphi\cos\kappa \\ \sin\kappa \\ -\sin\varphi\cos\kappa \end{bmatrix} = \begin{bmatrix} (X_V)_X\cos\varphi\cos\kappa+(Y_V)_X\sin\kappa-(Z_V)_X\sin\varphi\cos\kappa \\ (X_V)_Y\cos\varphi\cos\kappa+(Y_V)_Y\sin\kappa-(Z_V)_Y\sin\varphi\cos\kappa \\ (X_V)_Z\cos\varphi\cos\kappa+(Y_V)_Z\sin\kappa-(Z_V)_Z\sin\varphi\cos\kappa \end{bmatrix} \tag{13}$$

式中,$\boldsymbol{R}_b^V$ 为姿态参考坐标系到飞行坐标系的转换矩阵;$\boldsymbol{R}_V^E$ 为姿态参考坐标系到飞行坐标系的转换矩阵,(X_V),(Y_V),(Z_V) 的下标 X、Y、Z 表示飞行坐标系三轴单位向量分别在地心直角坐标系三轴方向的分量。

以传感器位置(Xs,Ys,Zs)、姿态(φ,κ)、地面点坐标(X,Y,Z)、传感器方位向和距离向系统误差(Δx_0,Δy_0)作为未知数,并对其进行线性化,得到 SAR 影像观测值误差方程式的一般形式:

$$\begin{cases} v_x = f_{xXs}\mathrm{d}Xs+f_{xYs}\mathrm{d}Ys+f_{xZs}\mathrm{d}Zs+f_{x\varphi}\mathrm{d}\varphi+f_{x\kappa}\mathrm{d}\kappa \\ \quad -f_{xXs}\mathrm{d}X-f_{xYs}\mathrm{d}Y-f_{xZs}\mathrm{d}Z+\Delta x_0-l_x \\ v_y = f_{yXs}\mathrm{d}Xs+f_{yYs}\mathrm{d}Ys+f_{yZs}\mathrm{d}Zs+f_{y\varphi}\mathrm{d}\varphi+f_{y\kappa}\mathrm{d}\kappa \\ \quad -f_{yXs}\mathrm{d}X-f_{yYs}\mathrm{d}Y-f_{yZs}\mathrm{d}Z+\Delta y_0-l_y \end{cases} \tag{14}$$

式中,(v_x,v_y)为像点坐标误差改正数,(l_x,l_y)为误差方程常数项,f_* 为误差方程系数。

从式(14)可以看出,SAR 影像的误差方程除线性化方法有所区别外,与共线方程的误差方程一般形式仍然是一致的。同时,从式(12)中的共面方程,容易建立多普勒误差对像点方位向坐标影响的误差传播公式:

$$\mathrm{d}x=\frac{-R\lambda}{2M_a|\boldsymbol{V}|}\mathrm{d}f_D \tag{15}$$

式(15)证明,多普勒参数值非 0 时对影像的几何定位的影响是不能忽略的。

4 SAR 影像与轨姿的联合平差模型

R-D 模型的定位通常以传感器位置(Xs,Ys,Zs)和速度(V_{Xs},V_{Ys},V_{Zs})作为外定向参数,研究表明,R-D 模型定位时高程向的速度对高程影响是非常敏感的(庞蕾,2006)。RCD 模型的外定向参数减少为 5 个,有利于提高稀少控制点条件下的空中三角

测量平差解算的稳定可靠性。采用如下低阶多项式作为姿态和位置的精化模型(程春泉和张继贤,2012):

$$\begin{cases} Xs = Xs_0 + a_0 + a_1 t \\ Ys = Ys_0 + b_0 + b_1 t \\ Zs = Zs_0 + c_0 + c_1 t \\ \varphi = \varphi_0 + f_0 + f_1 t \\ \kappa = \kappa_0 + g_0 + g_1 t \end{cases} \tag{16}$$

式中,Xs、Ys、Zs、φ 和 κ 为精化后的外定向参数,Xs_0、Ys_0、Zs_0、φ_0、κ_0 为外定向参数初值,a_i、b_i、c_i、f_i、g_i($i=0,1$)为轨道姿态修正多项式系数。

将精化模型代入构像模型,并对精化模型参数 a_i、b_i、c_i、f_i、g_i($i=0,1$)、地面点坐标参数 dX、dY、dZ 和传感器系统误差 Δx_0、Δy_0 参数进行线性化,容易得到以上述参数为未知数的误差方程。

本文新增的传感器方位向和距离向系统误差改正参数(Δx_0,Δy_0),可作为 SAR 传感器的几何定标检校参数。建立两种区域网平差模型,第一种以常规传感器位置和姿态精化模型参数、地面点坐标为未知数的区域网平差模型:

$$\begin{cases} \boldsymbol{V}_{xy} = \boldsymbol{B}_g g + \boldsymbol{B}_t t - \boldsymbol{L}_{xy} & \text{权}:P_{xy} \\ \boldsymbol{V}_g = \boldsymbol{E}_g g - \boldsymbol{L}_g & \text{权}:P_g \\ \boldsymbol{V}_t = \boldsymbol{E}_t t - \boldsymbol{L}_t & \text{权}:P_t \end{cases} \tag{17}$$

第二种模型在第一种基础上另外加上自检校参数 s(Δx_0,Δy_0)作为未知数和观测值:

$$\begin{cases} \boldsymbol{V}_{xy} = \boldsymbol{B}_g g + \boldsymbol{B}_t t + \boldsymbol{B}_s \boldsymbol{s} - \boldsymbol{L}_{xy} & \text{权}:P_{xy} \\ \boldsymbol{V}_g = \boldsymbol{E}_g \boldsymbol{g} - \boldsymbol{L}_g & \text{权}:P_g \\ \boldsymbol{V}_t = \boldsymbol{E}_t \boldsymbol{t} - \boldsymbol{L}_t & \text{权}:P_t \\ \boldsymbol{V}_s = \boldsymbol{E}_s \boldsymbol{s} - \boldsymbol{L}_s & \text{权}:P_s \end{cases} \tag{18}$$

式(17)、(18)中,$\boldsymbol{V}_{xy}$、$\boldsymbol{V}_g$、$\boldsymbol{V}_t$ 和 $\boldsymbol{V}_s$ 分别为像点坐标、地面点坐标、POS 观测值、检校参数观测值的误差方程,$\boldsymbol{g}$ 为地面点坐标增量未知数 [dX,dY,dZ],$\boldsymbol{t}$ 为轨道姿态精化模型多项式系数未知数 a_i、b_i、c_i、f_i 和 g_i($i=0,1$),$\boldsymbol{s}$ 代表 SAR 传感器检校系统误差未知数向量(Δx_0,Δy_0),$\boldsymbol{B}_g$、$\boldsymbol{B}_t$、$\boldsymbol{E}_g$、$\boldsymbol{E}_t$ 和 $\boldsymbol{E}_s$ 为未知数的系数矩阵。

5 机载 SAR 影像的定位试验与分析

5.1 试验数据

试验区选在河南登封市郊,试验区面积为东西向和南北向各 13 km,地形高程为 230—440 m,属丘陵和山地地形。采用中国测绘科学研究院研制的多波段多极化干涉极化 SAR 测图系统(CASMSAR)(Zhang,2012)获取的 X 波段机载 SAR 数据。有东向航线 6 个航带,西向航线 5 个航带,每航带有 9—10 景影像,共有东向影像 55 景,西向影像 44 景。SAR 成像多普勒参数值为 -600—600 Hz,不同航带差异较大;方位向和斜距向像元大小分别为 0.31 m 和 0.25 m,其实际地面分辨率约为 0.5—1.0 m;SAR 波长为 0.03 m;近距端斜距 2600 m 附近,远距端在 7500 m 附近;飞行航高约 3000 m。图2(a)(b)分别显示了东向和西向航线影像相互间的关系,图 3 显示了 SAR 影像的某个局部。

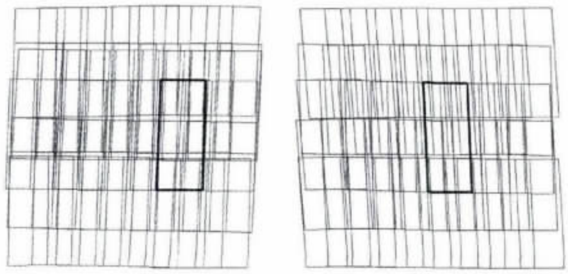

(a) 东向航线影像 (b) 西向航线影像

图 2 同一区域的东西向航线区域网影像
(粗线框为一景影像范围)

图 3 CASMSAR 系统获取的机载 SAR 影像局部

5.2 试验

(1)单片定向

选取其中一景影像,以影像中的原始辅助数据为定向参数值(该景影像的成像多普勒频率为 -322 Hz)。分别以 Lebel F 模型、R-D 模型、RCD 模型和 R-Cp 模型进行无控制点条件下的单片定向试验,单纯从构像几何的角度,考察非 0 多普勒 SAR 影像采用不同模型进行定向的差异(表 1)。R-Cp 模型定向采用的姿态俯仰角为 -0.785°、偏航角 -3.44°,取自该景影像获取期间的原始 POS 观测值。R-D 模型距离向定向残差计算方法与 RCD 模型相同,方位向残差 v_x 的计算仿照文献(程春泉和张继

贤,2012),将式(1)中多普勒方程两边同时乘以系数 $c=\lambda R/(2|V|M_a)$,将其转换为像点坐标 x 为因变量的显函数形式,得到显函数形式的 R-D 式(19),通过其线性化后的误差方程计算;Leberl 方程与 R-D 方程定向残差计算方法相同,但 f_D 值取恒 0。

$$\begin{cases} x = 2c\cdot[(X-Xs)V_X+(Y-Ys)V_Y+(Z-Zs)V_Z]/(\lambda R_j)-c\cdot f_D=0 \\ y = [\sqrt{(X-Xs)^2+(Y-Ys)^2+(Z-Zs)^2}-R_0]/M_r \end{cases} \tag{19}$$

表 1 不同模型单片定向精度统计 /像元

点号/距离向坐标	P01		P02		P03		P04		P05	
像点坐标(行/列)	7454	4502	4867	8359	4358	10759	54	12465	662	17916
误差方向	V_x	V_y	V_x	V_y	V_x	V_y	V_x	V_y	V_x	V_y
Leberl F	485.33	7.43	605.23	9.95	684.58	10.75	734.60	11.10	914.93	11.87
R-D	2.75	7.43	-3.10	9.95	-1.97	10.75	-7.57	11.10	-4.85	11.87
R-Cp	175.52	7.43	39.36	9.95	-25.65	10.75	-76.22	11.10	-194.38	11.87
RCD	2.75	7.43	-3.10	9.95	-1.97	10.75	-7.57	11.10	-4.85	11.87

(2)自由网平差

分别以东向航线、东西向航线进行区域网平差,以式(17)模型进行无控制点的自由网平差,得到的结果统计于表 2 中定向参数为"状态参数"行、控制点数目为"0"的列中。作为比较,以未进行精化的原始定向参数对区域网中的影像进行立体定位,得到的统计中误差东向航线平面为 2.73 m、高程为 2.35 m,对向航线平面为 2.08 m,高程为 2.91 m。

表 2 不同定位模型和方法区域网平差精度统计 /m

	定向参数	控制点数目		0	1	4	5	9	15
东向航线	状态参数	控制点	平面		0.07	0.51	0.60	1.13	1.31
			高程		0.11	0.44	0.49	0.74	0.97
		检查点	平面	2.19	2.04	1.75	1.69	1.55	1.47
			高程	1.97	1.35	1.21	1.19	1.11	1.00
	状态参数+自检校参数	控制点	平面		0.19	0.39	0.43	1.06	1.31
			高程		0.17	0.33	0.40	0.78	0.93
		检查点	平面	2.14	2.03	1.61	1.58	1.50	1.44
			高程	1.91	1.22	1.10	1.06	1.01	0.95
		最大误差	平面	3.50	2.89	2.37	2.25	2.17	1.95
			高程	3.92	2.33	2.19	2.16	2.05	2.00
对向航线	状态参数	控制点	平面		0.02	0.39	0.42	0.67	0.88
			高程		0.03	0.22	0.27	0.38	0.51
		检查点	平面	1.40	1.31	1.15	1.11	1.02	0.93
			高程	1.61	0.80	0.72	0.72	0.61	0.53
	状态参数+自检校参数	控制点	平面		0.09	0.41	0.49	0.75	0.83
			高程		0.03	0.38	0.40	0.42	0.49
		检查点	平面	1.30	1.17	1.05	0.97	0.92	0.87
			高程	0.59	0.58	0.55	0.53	0.50	0.46
		最大误差	平面	2.30	2.14	2.03	2.06	1.85	1.77
			高程	1.19	1.11	1.02	0.99	0.92	0.89

(3)不同控制点区域网平差

与试验(2)一样，分别以东向航线、东西向航线进行区域网平差，但在测区布设1—15个数目不等的地面控制点，考察不同控制点对影像区域网平差精度的影响，所得的结果统计于表中。其中1个控制点时置于测区中心位置，4个控制点时置于靠近测区的四角位置，5个控制点时置于测区中心和四角位置，9、15个控制点时较均匀分布于测区。结果列于表2“状态参数”行、控制点数目为“1”、“4”、“5”、“9”、“15”的列中。

(4)带有自检校参数的机载SAR区域网平差

将RCD误差方程中的Δx_0、Δy_0为传感器的自检校参数，利用式(18)，以试验(2)(3)中相同的数据分别利用0—15个控制点进行自由网与区域网平差试验，统计得到的控制检查点精度统计于表2“状态参数+自检校参数”栏中。

5.3 试验分析

(1)基于原始定向参数的R-D模型定向结果可以看出，本文试验影像在方位向存在的误差较小，在距离向存在的误差较大；但方位向的标准差要大于距离向标准差，表明影像距离向误差存在较强的系统性，方位向误差存在较大的随机性。

(2)从定向试验可以看出，当SAR影像成像多普勒频率较大时，不同构像模型的定向误差存在非常大的差异，R-D与R-P模型精度最好，且两者定向误差完全相同，R-Cp模型次之，Leber F模型最差。

(3)在稀少或无地面控制点的情况下，通过平差，平面和高程精度相对于原始定向参数的定位结果均有提高，但相同条件下带有自检校参数的区域网平差精度高于未带自检校参数的区域网平差精度，采用对向观测的SAR影像区域网平差精度高于同向航带的SAR影像区域网精度。

(4)随着控制点数目的增加，不同条件下检查点的定位精度也相应提高，但在稀少控制点条件下定位精度的提高并不快，原因是影像存在较大的随机误差，导致控制点对区域网影像的控制难以远距离传播，控制点对影像的控制范围有限。

(5)单独东向航线平差时，定位精度不是很理想，原因主要是影像选点误差和随机误差对小基高比立体影像的高程影响较大，表明生产应用中还需要在改善成像清晰度和减少影像变形随机误差上作进一步的努力。

(6)对向条带影像参加平差且采用自检校平差模型时，稀少或无地面控制点的条件下即有较高的精度，表明这种平差方法可以有效消除传感器或成像过程中引入的系统误差，且控制点数目达到5个时，满足1∶5000和1∶10000测图丘陵和山区区域网加密精度要求(AQSIQ和SAC,1992)。

6 结论

在前面工作的基础上(程春泉 等2012;程春泉和张继贤,2012)，以传感器位置和姿态作为定向参数，分别构建了真实孔径和合成孔径侧视雷达影像的几何构像距离—共面方程，通过侧视雷达影像与卫星轨道姿态或机载POS数据的联合平差处理，较系统地论述了稀少控制点条件下机、星载侧视雷达遥感影像的几何纠正、立体定位和区域网平差模型的技术和方法。距离—共面(平面或锥面，Range-Coplanarity或Range-CoCone，R-Cp或R-Cc)方程(程春泉和张继贤,2012)可用于真实孔径雷达影像、按波束中心过目标点多普勒成像的SAR影像及按常量多普勒成像的SAR影像，而考虑多普勒参数的距离共面方程RCD可应用于所有R-D模型成像的真实孔径和SAR影像。

相比R-D几何模型，本文建立的RCD几何模型减少了定向参数的数目，有利于降低定向参数间的相关性，提高稀少控制点条件下的影像平差解算的稳定性;SAR影像的摄影测量仍能吸收一些光学线阵影像成熟的数字摄影测量技术和方法，实现了SAR影像数据和POS数据的联合平差处理;自检校参数的加入，对提高稀少或无控制点几何检校精度较差的SAR传感器影像定位精度，有重要的作用。同时表明，随着机载SAR测图系统数据获取性能和机载SAR成像质量的进一步提高，影像定位精度虽仍有提升的空间，但稀少控制条件下机载SAR空中三角测量精度已达到1∶5000和1∶10000丘陵和山区航摄测图内业加密规范要求，机载SAR将逐渐应用于大比例尺测图生产应用中。

参考文献(References)

国家质量监督检验检疫总局，中华人民共和国国家标准. 1992. 1∶5000、1∶10000地形图航空摄影测量内业规范. GB/T 13990－92

程春泉，张继贤. 2012. 侧视雷达影像距离—共面模型严密定位. 遥感学报，16(5)：881－894

程春泉，张继贤，邓喀中，张力. 2012. 雷达影像几何构像距离—共面方程. 遥感学报，16(1)：38－49

DLR (The German Aerospace Center). 2007. CAF-Cluster Applied Remote Sensing. TerraSAR-X Ground Segment Level 1b Product Format Specification. http://www. astrium-geo. com/ files/pmedia/public/r460_9_030201_level - 1b-product - format - specification_1. 3. pdf

黄国满，岳昔娟，赵争，范洪冬. 2008. 基于多项式正射纠正模型的机载 SAR 影像区域网平差. 武汉大学学报(信息科学版)，33(6)：569 - 572

Johnsen H, Lauknes L and Guneriussen T. 1995. Geocoding of fast-delivery ERS-1 SAR image mode product using DEM data. International Journal of Remote Sensing, 16(11): 1957 - 1968 [DOI: 10.1080/01431169508954532]

马婧，尤红建，龙辉，丁赤飚. 2010. 一种新的稀少控制条件下机载 SAR 影像区域网平差方法的研究. 电子与信息学报，32(12)：2842 - 2847

Toutin T. 2003. Path processing and block adjustment with RADARSAT-1 SAR images. IEEE TGARS, 41(10): 2320 - 2328 [DOI: 10.1109/TGRS.2003.814661]

庞蕾. 2006. 机载合成孔径雷达空中三角测量方法的研究. 青岛：山东科技大学：20 - 46

袁修孝，吴颖丹. 2010. 缺少控制点的星载 SAR 遥感影像对地目标定位. 武汉大学学报(信息科学版)，35(1)：88 - 91

张过，墙强，祝小勇，唐新明. 2010. 基于影像模拟的星载 SAR 影像正射纠正. 测绘学报. 39(6):554 - 559

Zhang J X, Zhao Z, Huang G M and Lu Z. 2012. CASMSAR: An Integrated Airborne SAR Mapping System. PHOTOGRAMMETRIC ENGINEERING & REMOTE SENSING (11):1111 - 1114